Acta Biomaterialia 6 (2010) 2172–2180

Contents lists available at ScienceDirect

Acta Biomaterialia

journal homepage: www.elsevier.com/locate/actabiomat

Synchrotron X-ray diffraction study of load partitioning during elastic deformation of bovine dentin

A.C. Deymier-Black [a,*], J.D. Almer [b], S.R. Stock [c], D.R. Haeffner [b], D.C. Dunand [a]

[a] Department of Materials Science and Engineering, Northwestern University, Evanston, IL 60208, USA
[b] Advanced Photon Source, Argonne National Laboratory, Argonne, IL 60439, USA
[c] Department of Molecular Pharmacology and Biological Chemistry, Feinberg School of Medicine, Northwestern University, Chicago, IL 60611, USA

ARTICLE INFO

Article history:
Received 24 August 2009
Received in revised form 10 November 2009
Accepted 11 November 2009
Available online 16 November 2009

Keywords:
Collagen
Hydroxyapatite
Mechanical properties
X-ray diffraction
Dentin

ABSTRACT

The elastic properties of dentin, a biological composite consisting of stiff hydroxyapatite (HAP) nanoplatelets within a compliant collagen matrix, are determined by the volume fraction of these two phases and the load transfer between them. We have measured the elastic strains in situ within the HAP phase of bovine dentine by high energy X-ray diffraction for a series of static compressive stresses at ambient temperature. The apparent HAP elastic modulus (ratio of applied stress to elastic HAP strain) was found to be 18 ± 2 GPa. This value is significantly lower than the value of 44 GPa predicted by the lower bound load transfer Voigt model, using HAP and collagen volume fractions determined by thermo-gravimetric analysis. This discrepancy is explained by (i) a reduction in the intrinsic Young's modulus of the nano-size HAP platelets due to the high fraction of interfacial volume and (ii) an increase in local stresses due to stress concentration around the dentin tubules.

1. Introduction

Dentin, the main component of teeth, is a composite with a complex hierarchical structure consisting of nanocrystalline hydroxyapatite (HAP) platelets embedded within an amorphous protein matrix (mostly collagen, with some phosphoproteins), along with fluid-filled pores and dentinal tubules. These dentinal tubules (1–2.5 μm diameter), hollow or protein filled tubes that radiate from the pulpal cavity to the dentin surface, are surrounded by a mineralized collagen matrix of intertubular dentin (ITD). Within this matrix region and bordering each tubule is a 0.5 μm collar of peritubular dentin (PTD), which is somewhat more mineralized than the surrounding IDT [1–4]. The tubule center to center spacing is 5–10 μm, making them a significant feature in the dentin structure [4]. This complex composite microstructure of dentin, when combined with enamel, makes teeth some of the strongest, toughest and most resilient bio-composites. Much research has been devoted to the issue of crack nucleation and propagation in teeth, in particular the interplay between the tough but weak dentin and the brittle but strong enamel, which is relevant to the ability of teeth to mitigate crack propagation during shock or fatigue loading associated with occasional impact or long-term mastication [5–13]. A simpler, but no less important, issue relates to the elastic behavior of teeth under quasi-static loading (e.g. during biting or chewing), where load transfer is expected to occur between the stiff HAP platelets and the much more compliant protein matrix within the dentin. A better understanding of the micromechanics of load transfer within dentin may lead to better prosthetics and dental fillings and could also shed light on the mechanical evolution associated with microstructural changes within dentin due to aging, disease or injury.

Many studies have been conducted to measure the mechanical properties of dentin and enamel, namely Young's modulus, Poisson's ratio and failure stress, in the bulk (e.g. by compressive testing [14–16], ultrasonic measurements [15,17,18]) or over smaller volumes (e.g. by micro- or nano-indentation [19–22]). With these methods the overall mechanical properties of dentin as a composite can be measured, but the mechanical interaction between the two constitutive phases (the HAP crystals and the collagenous protein matrix) cannot be captured. During elastic loading of dentin, stresses are expected to be transferred to the stiff, strong HAP plates from the surrounding compliant collagen matrix. This will result in an increase in strain in the HAP phase and a concomitant decrease for the collagen phase, as compared with the strains that would have been developed upon loading of each pure phase. Load partitioning between the reinforcement and matrix phases has been extensively studied in synthetic metal matrix composites by synchrotron X-ray diffraction. This method allows the independent measurement of lattice strains in each of the crystalline phases of the composite during mechanical loading [23–25]. Recently this method has been applied to measure, during in situ

* Corresponding author. Tel.: +1 847 491 5933; fax: +1 847 491 7820.
E-mail address: alixdeymier2010@u.northwestern.edu (A.C. Deymier-Black).

1742-7061/$ - see front matter © 2010 Published by Elsevier Ltd. on behalf of Acta Materialia Inc.
doi:10.1016/j.actbio.2009.11.017

compressive deformation, elastic strains in the HAP phase in canine and bovine bone [26–29] as well as in deer antler [30]. In teeth, however, synchrotron X-ray radiation has only been used for imaging and mineral density measurement via micro-computed tomography (micro-CT) [31–37].

In this paper we apply synchrotron X-ray diffraction to determine elastic strains present in the HAP phase of dentin during compressive loading. These measurements were performed on the dentin of an entire tooth cross-section, and the results are discussed in terms of the load partitioning expected to occur between the HAP platelets and the surrounding protein matrix.

2. Materials and methods

2.1. Dentin preparation

The lower jaw of an 18-month-old cow was extracted and collected at the Aurora Packing Company (Aurora, IL) 2–3 h after death and immediately stored on ice. The first right erupted deciduous incisor was removed from the jaw with dental tools within a few hours of collection. The incisor was washed five times, for 20 min each, in phosphate-buffered saline (PBS) with 5% penicillin–streptomycin–amphotericin disinfectant solution (Invitrogen, Carlsbad, CA). It was then soaked in 5% NaOCl solution at room temperature overnight, followed by extensive washing in distilled water to remove any pulp or remaining surface organic matter. Although there is evidence that such treatments may remove collagen from the surface dentin [38–40], major effects on the diffraction results are unlikely, as the total sampling volume is expected to be much larger than any small deproteinated surface area. The disinfected incisor was then placed in PBS containing 50% glycerol and stored at −80 °C. While glycerol is known to cause the destabilization of collagen fibrils while stabilizing the collagen helix [41–43], it has been shown that all of the effects of glycerol on the mechanical properties of collagen are fully reversible upon rehydration [44]. Further evidence from unpublished data shows that similar tests done on dentin samples that were unbleached and not treated with glycerol showed similar stiffness values to those found here. Finally, freezing of the dentin samples was expected to have little to no effect on the mechanical properties of dentin [45–47].

The incisor was later transferred to a −20 °C freezer to thaw the PBS/glycerol solution. Upon thawing the tooth was cut within the root section into a 7.5 mm tall pseudo-cylinder with the original cross-section of the tooth. A first cut was made 11 mm below the gum line, perpendicular to the direction of growth, using a low speed diamond saw (Isomet 1000, Buehler, Lake Bluff, IL). A second cut was made 8 mm higher (3 mm below the gum line) parallel to the initial cut (±0.023 mm). The tooth was kept hydrated with PBS solution during mounting on the diamond saw and with distilled water during the cutting process. The final sample was an oblong, hollow section of the root with cross-sectional elliptical axes of ~4 and 7 mm and an elliptical pulpal cavity with ~1 and 2 mm axes. A photograph of the sample is shown in Fig. 1 and a micro-CT image of the cross-section of the sample is shown in Fig. 2. The sample was placed in PBS and frozen at −20 °C until the synchrotron experiments could be performed.

2.2. Diffraction measurements

The high energy X-ray diffraction measurements were performed at beam-line 1-ID-C of the Advanced Proton Source (APS) at the Argonne National Laboratory (Argonne, IL). Uniaxial compressive loading of the dentin cylinder was carried out using a custom built, screw-driven load frame. The sample was slowly deformed along its long axis at a cross-head displacement rate of 3.8 μm min^{-1} until failure. Force on the sample was determined using a 10 kN load cell. Wide angle X-ray scattering (WAXS) measurements were taken at five locations along the mesio-distal direction of the tooth for 30 s (during which the continuously recorded macroscopic strain of the sample increased by ~0.02% and the sample was exposed to approximately 20 kGy). The monochromatic 80.7 keV X-ray beam used for the diffraction measurements had a cross-sectional area of 50 × 50 μm, thus sampling an area large enough to contain multiple dentinal tubules with both ITD and PTD. This allows for measurement of the average HAP strain in dentin. A schematic of the experimental set-up is shown in Fig. 1. The five locations were spaced 1 mm apart and located at the vertical center of the dentin sample, with the beam traversing the sample from the lingual to the buccal side, as shown in Fig. 2. This figure also shows that a thin layer of cementum surrounded the dentin. The HAP WAXS rings were recorded using a GE Revolution 41RT Flat panel digital X-ray detector (General Electric, Waukesha, WI) with a diameter of 400 mm placed at a sample to camera distance of 1981 mm. A disk of pure pressed ceria powder (CeO_2, NIST Standard Reference Material SRM-674a), inserted at the beginning and end of the diffraction series, was used as a standard. During the entire experimentation time the sample was kept hydrated with PBS.

2.3. Micro-CT

After diffraction measurements the sample was imaged by micro-CT using both a synchrotron system at the APS and a laboratory system at Northwestern University. For the five months separating the diffraction and the tomography measurements the sample was maintained hydrated in PBS and frozen at −20 °C. The sample was then taken to sector 2-BM-B of the APS where it was thawed, and mounted in a PBS filled plastic tube. The tomography was done using the standard configuration of station 2-BM [48,49], at an X-ray energy of 26 keV, with 0.125° rotation increment between projections and with magnification lens of 2.5× and 1.25× (producing reconstructions with 2.8 and 5.6 μm isotropic volume elements,

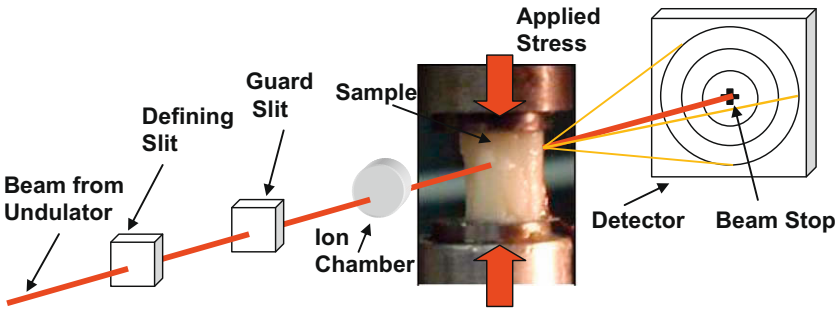

Fig. 1. Schematic of the experimental diffraction set-up showing a photograph of the bovine dentin sample. The height of the sample is 7.5 mm.

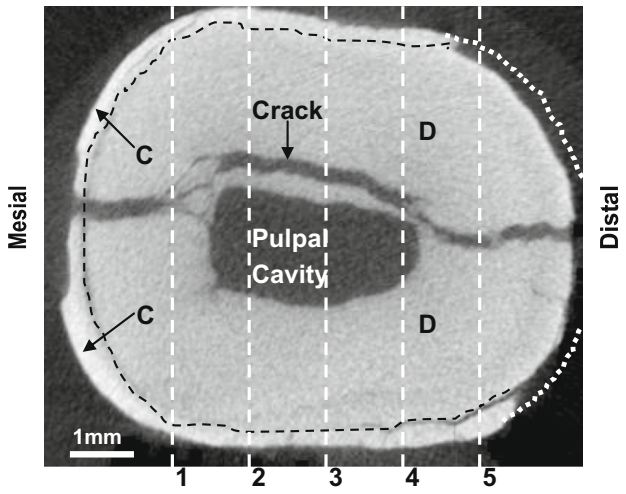

Fig. 2. Laboratory micro-CT image of the tooth middle cross-section containing the five locations (numbered dotted lines) at which diffraction patterns were obtained. Tooth components are marked C for cementum and D for dentin. The crack formed after the last diffraction measurements. The missing cementum on the right side of the image (white dotted line) spalled off the sample after the diffraction measurements had been completed due to drying effects and sample damage due to loading. The bright appearance of the cementum in this image is due to beam hardening, which causes the outside shell of the sample to appear brighter as compared with the center. In fact, absorption coefficient measurements showed that there was no measurable difference in mineralization between the dentin and the cementum in this sample.

respectively). The lower resolution scan covered the entire specimen cross-section, while small sections of the cementum were out of the field of view in the higher magnification scan. Only one slice was analyzed for each magnification, at a position equivalent to the plane sampled during the in situ loading measurements. In the high resolution slice linear attenuation coefficients were measured for five different locations associated with the sampling volumes in the dentin and cementum of the sample using ImageJ software [50].

Accurate information about the cross-sectional area of the sample was obtained through laboratory micro-CT measurements using a Scanco Medical MicroCT 40 system (Scanco Medical, Wayne, PA). The microfocus X-ray tube was operated at 70 kV and 114 μA, and the beam passed through a 0.13 mm thick Be window on the X-ray tube and through a 0.50 mm thick Al filter before encountering the sample. With this cone beam system 500 projections were collected over a 0.300 s integration time for each projection, with a 1024 pixel diameter. Reconstruction was on a 1024×1024 grid with 20 μm voxels (volume elements). Only one slice equivalent to the previous synchrotron micro-CT and in situ deformation measurement cross-sections was analyzed.

The cross-sectional area of the specimen at the approximate position where the X-ray scattering measurements were collected was determined from reconstructed cross-sections using the Scanco software suite. In this determination the standard threshold for bone histomorphometry suggested by the manufacturer, verified for bone of adults of various species in the scanner used in this study and confirmed for bovine dentin, was used to differentiate the mineralized tissue from the other less absorbing material, such as the PBS and plastic container. Specifically, the threshold was 200 on a scale of 0–1000, corresponding to linear attenuation coefficients of 0–8 cm^{-1}, respectively.

2.4. Diffraction analysis

A typical WAXS pattern for the HAP phase is shown in Fig. 3. The near uniform intensity of the diffraction ring is evidence that the

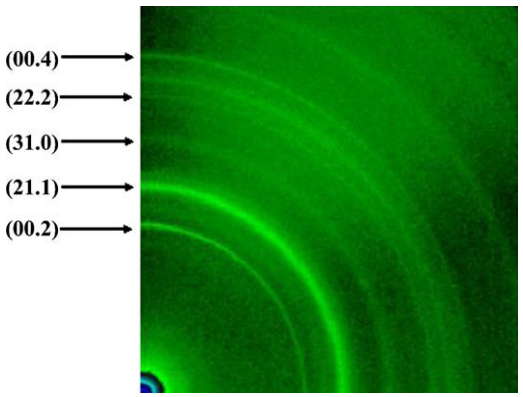

Fig. 3. Representative WAXS pattern (quarter of detector area) for the dentin sample (point 4 at a stress of 91 MPa).

HAP crystals in the dentin sample are much smaller than the diffraction volume and only weakly textured [25,51]. To determine the lattice spacing, procedures similar to those presented in Young et al. [23,25,53], Daymond et al. [51] and Wanner and Dunand [52] were followed. First, the beam center, detector tilt and sample to camera distance were determined with the program Fit2D [54,55] using the CeO_2 (200) and CeO_2 (333) reflections of the ceria standard, providing 'calibration parameters'. These parameters were then used to convert the sample diffraction patterns from polar to Cartesian coordinates. A MATLAB (www.mathworks.com) algorithm was then employed to fit specific crystallographic reflections, in this case the HAP (00.2), HAP (22.2) and HAP (00.4) reflections, as also chosen by Almer and Stock [27,28]. The profile of the peaks as a function of radial position was fitted using a pseudo-Voigt function to find the average center of the peak intensity at each angular position (η). The radial location of this peak center (R) was then converted into a d spacing using calibration parameters and the X-ray wavelength. To obtain a HAP lattice strain, the stress-free point (R_0) was determined by plotting R vs. $\sin^2(\Psi)$, where $\Psi = \eta\theta\cos(\eta)$ and θ is the Bragg angle, for all stresses and determining the point of intersection. The internal lattice strain of a specific reflection of HAP in the dentin can then be determined as $\varepsilon(\eta) = (R_0 - R(\eta))/R_0$. From plots of $\varepsilon(\eta)$ vs. η the axial and transverse strain components $e_{11} = \varepsilon(90^\circ)$ and $e_{22} = \varepsilon(270^\circ)$, respectively, can be found using equations derived by He and Smith for two-dimensional detectors [56].

2.5. Phase fraction determination

After X-ray diffraction the dentin sample was cut into 16 specimens with a volume of 1–3 mm^3 (and masses of 3–10 mg) using a low speed diamond saw. The specimens were maintained hydrated during and after the cutting process. Thermo-gravimetric analysis (TGA) measurements were performed using a Mettler Toledo TGA/SDTA 851^e Thermogravimetric analyzer. The samples were maintained hydrated in PBS until immediately preceding measurement, when they were blotted dry and placed in an alumina pan. Each sample was heated from ambient temperature to 650 °C at a rate of 10 °C min^{-1} and maintained at the maximum temperature for 5 min. Weight fractions of water and collagen were determined from the accumulated weight loss between 20 and 250 °C and between 250 and 600 °C, respectively, according to Holager [57]. Literature values of collagen and HAP density, 1.34 and 3.16 g cm^{-3}, respectively [58,59], were then used to convert weight fractions to volume fractions.

Inductively coupled plasma mass spectroscopy (ICP-MS) measurements of calcium and phosphorus content in a sample taken

from the same root were performed at A&L Laboratories (Memphis, TN) to independently assess the HAP fraction. The sample was sectioned in the same manner as that used during the in situ deformation experiments. The sample had a wet blotted mass of 253 mg and a volume of 105 mm^2, as determined from Archimedes measurements. The sample mass was determined from 10 measurements of the wet sample after surface blotting, from a dry samples after air drying for 12 h and covering with a thin layer of silicon vacuum grease, and from the same dry and greased sample immersed in water. The grease acts to fill any open porosity on the surface to obtain an accurate sample volume. After weighing the sample, it was crushed into a large grained powder and sent for chemical analysis as described above.

3. Results

Values of cross-head displacement and applied stress were used to obtain a plot of stress vs. displacement for the macroscopic sample. This macroscopic stress–displacement curve was linear until failure (which occurred at an applied stress of 107 MPa), indicating that the dentin specimen acted purely elastically. The failed sample exhibited a single branched crack traversing the full height of the sample at an angle of 45°, visible in Fig. 2.

Fig. 4 shows, for location 3, plots of HAP elastic lattice strains parallel (e_{11}) and perpendicular (e_{22}) to the loading direction as a function of the applied stress (σ), calculated from the applied force divided by the cross-sectional area of the sample as determined by micro-CT. These plots are linear, with slopes defined as the apparent in situ elastic modulus of the HAP phase in the presence of protein, water and porosity in dentin. Best fit to the data in Fig. 4 resulted in HAP apparent moduli values of $E_{11}^{app} = \sigma/e_{11} = 17$ GPa in the longitudinal direction, parallel to the loading direction and $E_{22}^{app} = \sigma/e_{22} = 78$ GPa in the transverse direction, perpendicular to the direction of loading. The HAP strain at a 45° angle to the loading direction (e_{12}) was approximately equal to 0 at all stresses, as expected for uniaxial loading.

The residual strains present in the material at zero applied stress in Fig. 4 were -1930 με for e_{11} and 450 με for e_{22}. The average values for all of the points were -1710 ± 80 με for e_{11} and 410 ± 110 με for e_{22}. Both values were close to those found in canine fibula ($e_{11} = -1440$ με and $e_{22} = 570$ με) [27].

Values for E_{11}^{app} and E_{22}^{app} are plotted in Fig. 5 for the five locations studied. The value of E_{11}^{app} was higher on the mesial side of the specimen as compared with the center, while the values for E_{22}^{app} were constant, within experimental error. The variation in E_{11}^{app} was probably not significant, given various sources of uncertainty not captured by the purely statistical errors (approximately ±0.5 GPa) shown on the plot. Possible systematic errors include variations in the cementum/dentin ratio, local variations in the HAP content, non-uniform uniaxial loading due to the unmachined shape of the sample or slight deviation in the parallelism of the sample faces. The average effective moduli for the five locations were $E_{11}^{app} = 18 \pm 2$ GPa and $E_{22}^{app} = 83 \pm 12$ GPa. Also plotted in Fig. 5 is the apparent Poisson's ratio of HAP in dentin ($\nu^{app} = E_{11}^{app}/E_{22}^{app}$), which has an average value of 0.22 ± 0.03.

Use of an entire tooth cross-section in the present study demonstrates that high energy scattering methods may be used for in situ stress measurements for entire extracted teeth (rather than small machined dentin specimens). Measurements may even be possible on the tooth–ligament–bone system of the mandible, opening the possibility of in vivo measurements on small animal models.

Fig. 6 shows a TGA plot graphing the mass of the dentin sample as a function of temperature. Two plateaux at ~220 and 600 °C were interpreted as corresponding to the end of water evaporation and collagen decomposition, respectively, from which volume per cents of each phase were then calculated as $38.5 \pm 1.4\%$ for HAP, $31.0 \pm 1.8\%$ for water and $30.5 \pm 1.89\%$ for collagen, as averaged from the five measurements. The measured Ca/P ratio (determined by ICP-MS) was 1.7 and was close to the stoichiometry of $Ca_{10}(OH)_2(PO_4)_6$, and the corresponding HAP volume fraction was $35.2 \pm 3.8\%$, in good agreement with the TGA results. The linear attenuation coefficients measured from the synchrotron micro-CT data showed no significant variation at the five measurement locations across the tooth. The average linear attenuation coefficient for the five points was $1.63 \times 10^{-3} \pm 2 \times 10^{-5}$ $voxel^{-1}$. This suggests that mineralization throughout the tooth was constant.

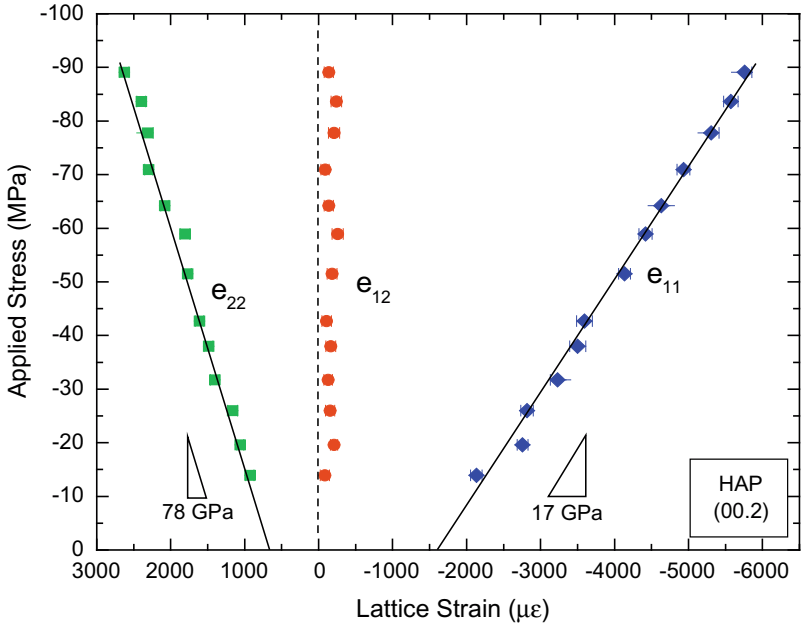

Fig. 4. Plot of applied compressive stress vs. longitudinal (e_{11}) and transverse (e_{22}) elastic lattice strain for HAP for location 3. The slopes are the HAP apparent elastic moduli: $E_{11}^{app} = 17$ GPa and $E_{22}^{app} = 78$ GPa.

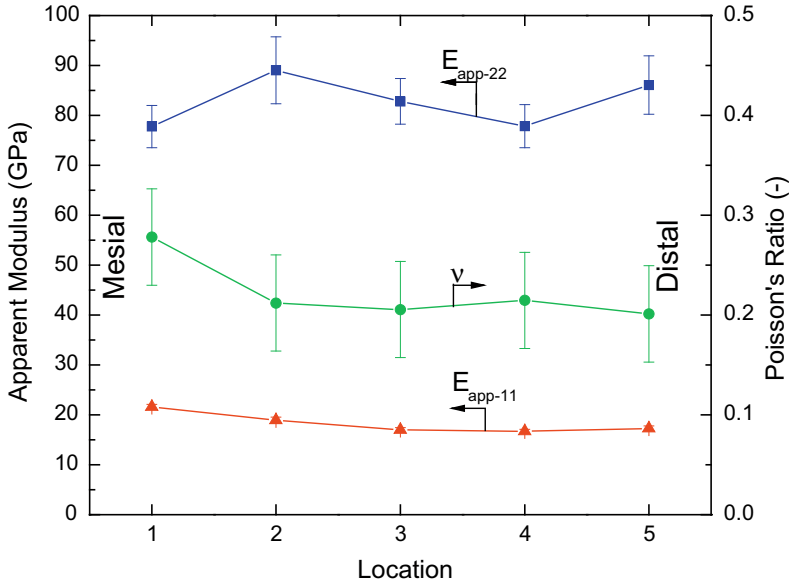

Fig. 5. Plot of apparent moduli E_{11}^{app} and E_{22}^{app} and Poisson's ratio ν as a function of location across the tooth from the mesial to the distal edge. Error bars for E_{11}^{app} are present but not visible due to their small size. Average error for E_{11}^{app} was ±0.5 GPa.

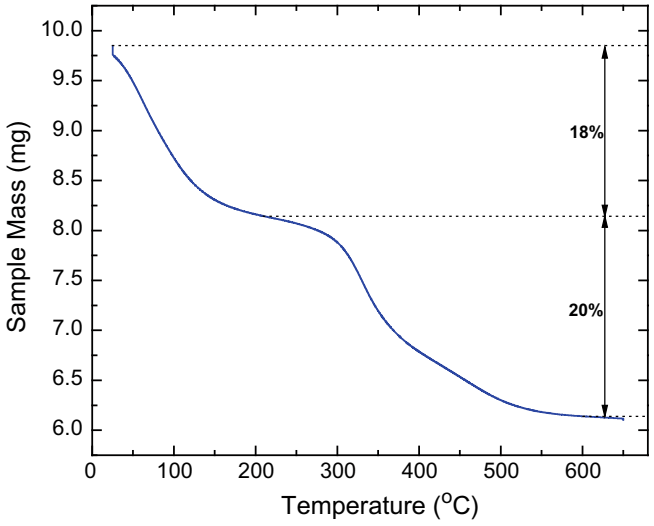

Fig. 6. Representative TGA plot for a small sample taken from the dentin specimen previously used for diffraction. The first and second plateau represent removal of water and collagen, respectively.

4. Discussion

4.1. Volume fraction determination

The volume fractions determined by TGA and ICP-MS measurements showed a lower percentage of HAP in the test sample as compared with the literature values of 45% HAP, 33% collagen and 22% water for mature human dentin [1–4]. Due to the many similarities between bovine and human dentin structure [60] and radiodensity [61,62] it would have been expected that they would also have similar compositions. This low level of mineralization in the present bovine sample may be due to it being part of a primary or deciduous tooth. Previous research has indicated that primary dentin is less calcified than its permanent counterpart [63,64]. This observation was supported by nano-indentation studies showing lower hardness in the deciduous teeth [1,65].

It is also possible that the primary tooth studied here was already affected by dental resorption [1,2,4] since the sample was extracted from the first incisor of an 18-month-old cow, which is usually shed around month 24 [66]. However, the condition of the tooth upon extraction and the presence of an intact cementum layer and thick root wall suggest that no obvious resorption was underway. As mineralized tissues are known for their variability from individual to individual, it is also possible that the specimen investigated here was from the low end of the distribution of dentin mineral levels found in the bovine population.

The presence of less mineralized cementum in the specimen might also be responsible for the unexpectedly low overall mineral level in the sample. Cementum is usually considered to be about 9% less mineralized than dentin in permanent human teeth (i.e. 41 vol.% HAP in cementum as compared with 45 vol.% in dentin) [19], and cementum comprises over 20% of the tooth cross-section in Fig. 2 and cannot be neglected. Micro-CT, however, showed no measurable difference in the attenuation coefficients of the two solid portions of the two tissues and, therefore, no difference in the mineralization of the two collagen–HAP phases. Instead, it showed that cementum has considerable porosity at the 10 μm level (presumably for attachment of periodontal ligaments anchoring the tooth to the mandible), porosity that is absent in the dentin. Therefore, it is not surprising that conventional measurements would show lower mineral content in the cementum compared with dentin, whereas the actual mineral levels within the two collagen–HAP materials would be comparable.

4.2. Diffraction measurements

The value of 107 MPa for the compressive failure stress was far less than the typical literature value of 275–300 MPa for permanent human dentin [14], or even 129 MPa for the ultimate tensile stress of permanent bovine dentin [67]. This low failure stress is likely due to size effects. The literature samples of solid 0.25–1.02 mm high cylinders of 0.25 mm diameter of dentin [14] were significantly smaller and contained fewer stress concentrators than the naturally shaped $7.5 \times 7 \times 4\text{mm}^3$ specimen used here. The decreased mineralization of deciduous bovine dentin as compared with permanent bovine dentin could also be responsible. The low

failure stress of 107 MPa also explains the reason for the strictly linear plots, as previous work has shown that human permanent dentin undergoes plastic deformation above a proportional limit of 166 MPa [14].

4.2.1. Apparent stiffness

The average value for the apparent in situ elastic modulus of HAP in dentin, $E_{11}^{app} = 18 \pm 2$ GPa, was lower than the apparent HAP elastic modulus reported previously. With the same techniques as presented here, Almer and Stock [28] measured $E_{11}^{app} = 32.8$ GPa in canine fibula with a mineral content of 36.5 vol.% and Akhtar et al. [30] found $E_{11}^{app} \approx 21$ GPa in fallow deer antler with a mineral content of 30.0 vol.%. This suggests that load transfer from the collagen phase to the HAP phase occurs to a greater extent in bovine dentine (thus reducing the apparent modulus), and this may be due to differences in microstructure and the ratio of collagen to fluid filled porosity, as well as size, structure and spatial distribution of the mineral platelets. The apparent Poisson ratio of HAP in dentin is quite close to the pure HAP Poisson ratio of 0.27 [68]. A lower bound for the apparent elastic modulus of HAP, E_{HAP}^{app} (corresponding to an upper bound for the stress, and thus elastic strain, carried by HAP for a given composite strain) was found using the Voigt composite model:

$$E_{HAP}^{app} = E_{HAP}V_{HAP} + E_{col}V_{col} + E_{H_2O}V_{H_2O} \quad (1)$$

where E_{HAP}, E_{col} and E_{H_2O} are the bulk elastic moduli of HAP, collagen and water, respectively, and V_{HAP}, V_{col} and V_{H_2O} are the volume fraction of these phases. In this model E_{HAP}^{app} has the same value as the overall composite modulus, since the strain in both the HAP phase and the composite are the same. Using the aforementioned experimental TGA phase volume fractions and literature values of $E_{HAP} = 114$ GPa, $E_{col} = 1$ GPa and $E_{H_2O} = 0$ GPa [69,70], Eq. (1) predicts a value of 44 GPa for E_{HAP}^{app}, which is more than twice our experimental value.

There are two main possible reasons for this discrepancy in the value of the apparent elastic modulus: (i) an increase in the local stress at the regions being measured; (ii) a decrease in the stiffness of the HAP crystals. These are described in what follows. A third hypothesis, which assumes that a fraction of the HAP phase is non-load-bearing, thus reducing the value of V_{HAP} in Eq. (1), can be eliminated. This is because this situation would result in asymmetric broadening of the diffraction peaks upon loading due to the variation in strain between the load-bearing and non-load-bearing HAP platelets. Such broadening was not observed at any of the five positions across the sample nor at any azimuthal angle, consequently eliminating this possibility.

4.2.2. Stress concentration effects

The first hypothesis considers that the stress to which the diffracting HAP platelets are subjected is higher than the average applied stress due to stress concentration near the tubules in dentin. Calculation of the apparent modulus assumes that the applied stress is evenly distributed throughout the sample. However, in this experiment the tubule long axes run perpendicular to the compression direction and thus produce local stress concentrations, magnifying the stress to which HAP platelets are subjected beyond the far field value. The strain reported in Fig. 4 is based on changes in the (00.2) diffraction ring diameter along the azimuth parallel to the loading direction. Since the (00.2) planes lay perpendicular to the *c* axis of the crystals (Fig. 7) this portion of the diffraction ring reflects only those HAP particles aligned with their *c* axis parallel to the direction of loading, i.e. those contained within collagen fibrils with their long axis parallel to the applied load. Collagen fibrils in dentin are mainly arranged with their long axis tangential to the tubule circumference and lie in the plane perpendicular to the tubule axes, as shown in Fig. 7 [71]. Therefore, the axially loaded collagen fibrils are most prevalent in the area besides the tubules (point A in Fig. 7), where stress concentrations are the highest, as compared with the top and bottom of the tubule (point B), where the magnitude of the stress is unchanged. As a result, the platelets contributing to the diffraction ring azimuth associated with the loading direction are those witnessing the highest stress concentration. To estimate the level of stress concentration, simple closed-form equations for a cylindrical hole in an infinite plate under compression were used [72]: the maximum stress concentration factor was 3, immediately next to the cylindrical tubule (point A), dropping to the far field value of unity away from the hole. Making the assumption that the axially arranged fibrils were mostly located at a distance of 1–5 μm from an average sized tubule of 1.2 mm diameter, the line average over the distance [AC] = 1–5 μm in Fig. 7 gives a mean stress concentration factor of ~1.8–1.2. Taking the average stress concentration factor of 1.5 increases the value of E_{HAP}^{app} to 27 GPa, which is still lower than the lower bound of 44 GPa previously calculated from Eq. (1).

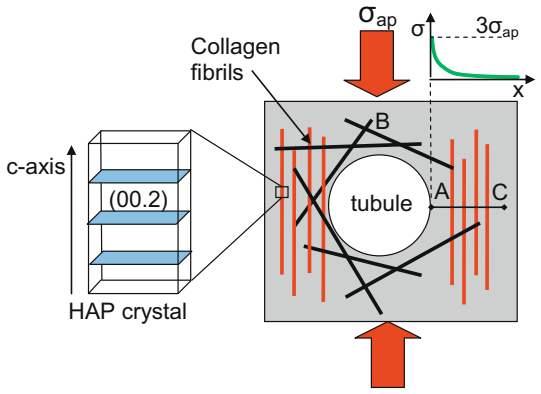

Fig. 7. A schematic of (00.2) planes in a HAP platelet, shown at left, illustrates how the preferentially sampled crystals were located in axially aligned fibers (highlighted in red). In turn, these fibers were most likely found besides the tubules (A) where the stress concentration was highest (see plot top right) as compared with the top and bottom of the tubule (B). Average stress concentration factors calculated over the distance [AC] = 1–5 μm are found to be in the range 1.2–1.8. (For interpretation of the references to colours in this figure legend, the reader is referred to the web version of this paper.)

4.2.3. Stiffness of nanosized HAP platelets

The second hypothesis considers the possibility that the reported literature values for the modulus of bulk, pure HAP ($E_{HAP} = 114$ GPa) may not apply to the present nanoscale HAP platelets. A low stiffness for nanoscale platelets can be justified by: (a) the presence of an amorphous or disordered layer on the surface of the platelets; (b) size effects related to the extreme thinness of the HAP platelets; (c) environmental effects. Each of these is discussed in the following paragraphs.

Although the presence of clear diffraction patterns proves that some of the HAP platelets were crystalline, it does not eliminate the possibility that a fraction of the HAP platelets were amorphous. The elastic modulus of amorphous HAP (created inorganically via a highly energetic process) has been reported as 70–80 GPa [73,74], which is significantly lower than that of crystalline HAP. This causes a decrease in the average stiffness of the platelets and a decrease in the apparent stiffness of the crystalline phase. X-ray and electron microscopy indicated that HAP nano-crystals formed by aqueous methods maintained an amorphous component, sometimes seen as a 1–2 nm thick coating on their surface [75,76]. Since studies suggest that crystalline biological HAP platelets may be formed from an amorphous precursor [77,78], it seems plausible

that a small amorphous layer may remain present in the platelets. The effect may be large because a single unit cell thick coating (~1 nm) on an average sized platelet of 4 × 20 × 70 nm represents over 56% of the total platelet volume. With a 34% decrease in the elastic modulus as compared with crystalline HAP (from 114 to 75 GPa), the presence of such an amorphous coating would decrease the overall platelet modulus to 92 GPa. Using a modified version of Eq. (1), in which $E_{HAP}V_{HAP}$ is replaced by $E^{C}_{HAP}V^{C}_{HAP} + E^{A}_{HAP}V^{A}_{HAP}$, where the superscripts C and A represent crystalline and amorphous HAP, respectively, the new calculated apparent elastic modulus of crystalline HAP in dentin drops from 44 to 36 GPa. This decrease is significant, but insufficient to match the stress–concentration corrected value of 27 GPa.

This amorphous effect may be further enhanced by increased disorder in the biological HAP. Fourier transform infrared spectroscopy and TGA studies on bone [79] and teeth [80] have shown that biological HAP in dentin has 2–3% of carbonate substitution, and this amount increases with age. These trigonal carbonates mostly substitute for tetrahedral phosphate structures within the crystal [81], causing the overall HAP structure to become disordered and the bonds to weaken. This decrease in crystallinity of the sample could be responsible for a decrease in the elastic modulus of the platelet. Although the low percentage of substitutions cannot explain the large discrepancy in the elastic modulus of the HAP crystals, it may contribute partially to this effect.

Secondly, a decrease in the elastic modulus of the HAP crystals may be caused by their nanometric size. It is well established that the elastic modulus of most materials changes significantly between a bulk macroscopic size and a nanoscopic size, due to the accentuated role of surfaces and interfaces in small volumes [82]. Most metal thin films with thicknesses below 30 nm show decreases in their elastic moduli due to interfacial effects, such as grain boundary sliding or the decreased modulus of grain boundaries [83–91]. Many fewer studies have been performed for the case of ceramics. However, it has been shown that diamond-like carbon thin films undergo a decrease in elastic modulus as their thickness decreases [92–94]. This decrease can be as much as 44% of the elastic modulus (360 GPa at 6 nm vs. 640 GPa at 125 nm thickness) [92]. Using semi-continuum models on platelike nanomaterials a 27% decrease in the modulus for NaCl was predicted for thin films with less than 10 atomic layers [95]. If the HAP nano-platelets with an amorphous layer underwent a similar decrease of ~30% due to size effects, then the HAP platelet stiffness becomes 65 GPa. This decreases the apparent modulus of HAP in dentin calculated from the modified equation (1) to 25 GPa, close to the stress–concentration corrected value of 27 GPa.

Some ceramics, such as ZnO, have shown an increase in the elastic modulus when made into 80 nm diameter nano-wires [96,97]. This increase was caused by the formation of a stiff outer layer during contraction of the near surface bonds [96,97]. This observation, apparently contradicting the assumptions of the previous paragraph, highlights the importance of the surrounding environment on the properties of materials with such high surface areas. For example, the elastic modulus of 150 nm thick SiO_2 films has been shown to decrease from 67 GPa when tested in a dry atmosphere to 57 GPa in a wet one [98]. This decrease is most likely due to surface bonding of hydroxyl groups [98]. In the case of HAP in dentin the surface is bound to water and hydroxyl groups [99], which can create a hydrated surface layer [100]. Furthermore, the elastic modulus of surface carbonate substituted HAP has been shown to decrease by approximately 12% when immersed in water [99]. These observations suggest that the surface of the HAP crystals in dentin may not only be amorphous, but also have a low elastic modulus due to interfacial surface behavior. The 12% decrease due to water addition would bring the HAP platelet stiffness to 57 GPa and the HAP apparent modulus to 22 GPa, which is between the measured value of 18 ± 2 GPa and the stress–concentration corrected value of 27 GPa.

In summary, although none of the above explanations independently explains the low apparent elastic modulus of the HAP in dentin, their combination forms a credible argument for such a discrepancy. The lower elastic modulus of biological HAP may also play an important role in increasing the toughness of dentin. With a decreased HAP stiffness the dentin will be better able to absorb large strains upon loading or impact, therefore maintaining the integrity of the entire tooth under harsh mechanical conditions. Also, the presence of an amorphous or hydrated layer surrounding the crystalline HAP may help create a gradient in stiffness between the collagen matrix and the HAP platelets, improving the ability to transfer load. These effects may be useful for the future development of tougher, more realistic dental materials.

5. Conclusions

The longitudinal apparent in situ Young's modulus of HAP was measured during elastic deformation of bovine dentin as 18 ± 2 GPa, using high energy X-ray diffraction. This value is much lower than the Young's modulus of bulk HAP, 114 GPa, indicative of substantial load transfer from collagen to HAP. Using experimentally measured volume fractions of HAP, collagen and water a lower bound model significantly overestimates the apparent modulus of HAP in dentin. This is explained by considering that: (i) X-ray diffraction measurements preferentially record strain in HAP platelets subjected to stress concentration near tubules; (ii) the stiffness of the HAP crystals within dentin may be much lower than in the bulk (57 vs. 114 GPa). The latter effect can be justified by considering the nanometric size, chemical composition and amorphous structure of the HAP in dentin. These conclusions show that the view of dentin as a simple composite of pure collagen and bulk HAP is too simplified and that the biological origin of tooth HAP, as well as its complex structure, must be taken into account.

Acknowledgements

The authors thank Prof. Arthur Veis (Northwestern University) for providing the tooth used for the in situ deformation and Dr. Francesco De Carlo of the Advanced Photon Source (APS) for help in collecting the synchrotron microcomputed tomography data at station 2-BM of the APS. They also thank Dr. Marcus Young (Northwestern University, now National Renewable Energy Laboratory) for his help at the beamline and for advice on data analysis. This research was performed at station 1-ID of XOR-APS at the APS, which is supported by the US Department of Energy, Office of Science, under Contract No. DE-AC02-06CH11357. Partial funding was provided to A.C.D. by a National Defense Science and Engineering Graduate Fellowship from the Department of Defense.

Appendix A. Figures with essential colour discrimination

Certain figures in this article, particularly Figs. 1 and 3–7, are difficult to interpret in black and white. The full colour images can be found in the on-line version, at doi: 10.1016/j.actbio.2009.11.017).

References

[1] Avery JK. Oral development and histology. New York: Theime Medical; 1994.
[2] Avery JK, Chiego DJ. The essentials of oral histology and embryology: a clinical approach. St. Louis (MI): Mosby; 2006.
[3] Brand RW, Isselhard DE. Anatomy of orofacial structures. St. Louis (MI): Mosby; 1998.
[4] Ten Cate AR. Oral histology: development, structure and function. St. Louis (MI): Mosby; 1980.

[5] Craig RG, Gehring PE, Peyton FA. Relation of structure to the microhardness of human dentin. J Dent Res 1959;38:624–30.
[6] El Mowafy OM, Watts DC. Fracture toughness of human dentin. J Dent Res 1986;65:677–81.
[7] Kahler B, Swain MV, Moule A. Fracture-toughening mechanisms responsible for differences in work to fracture of hydrated and dehydrated dentine. J Biomech 2003;36:229–37.
[8] Kruzic JJ, Nalla RK, Kinney JH, Ritchie RO. Crack blunting, crack bridging and resistance-curve fracture mechanics in dentin: effect of hydration. Biomaterials 2003;24:5209–21.
[9] Lin CP, Douglas WH. Structure–property relations and crack resistance at the bovine dentin–enamel junction. J Dent Res 1994;73:1072–8.
[10] Rasmussen ST, Patchin RE, Scott DB, Heuer AH. Fracture properties of human enamel and dentin. J Dent Res 1976;55:154–64.
[11] Rasmussen ST, Patchin RE. Fracture properties of human enamel and dentin in an aqueous environment. J Dent Res 1984;63:1362–8.
[12] Staninec M, Marshall GW, Hilton JF, Pashley DH, Gansky SA, Marshall SJ, et al. Ultimate tensile strength of dentin: evidence for a damage mechanics approach to dentin failure. J Biomed Mater Res 2002;63:342–5.
[13] Wang R. Anisotropic fracture in bovine root and coronal dentin. Dent Mater 2005;21:429–36.
[14] Craig RG, Peyton FA. Elastic and mechanical properties of human dentin. J Dent Res 1958;37:710–9.
[15] Kinney JH, Marshall SJ, Marshall GW. The mechanical properties of human dentin: a critical review and re-evaluation of the dental literature. Crit Rev Oral Biol Med 2003;14:13–29.
[16] Peyton FA, Mahler DB, Hershenov B. Physical properties of dentin. J Dent Res 1952;31:366–70.
[17] Kinney JH, Gladden JR, Marshall GW, Marshall SJ, So JH, Maynard JD. Resonant ultrasound spectroscopy measurements of the elastic constants of human dentin. J Biomech 2004;37:437–41.
[18] Vieira APGF, Hancock R, Dimitriu M, Limeback H, Grynpas MD. Fluoride's effect on human dentin ultrasound velocity (elastic modulus) and tubule size. Eur J Oral Sci 2006;114:83–8.
[19] Ho SP, Balooch M, Goodis HE, Marshall GW, Marshall SJ. Ultrastructure and nanomechanical properties of cementum dentin junction. J Biomed Mater Res A 2004;68:343–51.
[20] Tesch W, Eidelman N, Roschger P, Goldenberg F, Klaushofer K, Fratzl P. Graded microstructure and mechanical properties of human crown dentin. Calcif Tissue Int 2001;69:147–57.
[21] Angker L, Swain MV. Nanoindentation: application to dental hard tissue investigations. J Mater Res 2006;21:1893–905.
[22] Inoue T, Saito M, Yamamoto M, Debari K, Kou K, Nishimura F, et al. Comparison of nanohardness between coronal and radicular intertubular dentin. Dent Mater J 2009;28:295–300.
[23] Young ML, DeFouw JD, Almer JD, Dunand DC. Load partitioning during compressive loading of a Mg/MgB2 composite. Acta Mater 2007;55:3467–78.
[24] Mueller R, Rossoll A, Weber L, Bourke MAM, Dunand DC, Mortensen A. Tensile flow stress of ceramic particle-reinforced metal in the presence of particle cracking. Acta Mater 2008;56:4402–16.
[25] Young ML, Almer JD, Daymond MR, Haeffner DR, Dunand DC. Load partitioning between ferrite and cementite during elasto-plastic deformation of an ultrahigh-carbon steel. Acta Mater 2007;55:1999–2011.
[26] Akhtar R, Daymond MR, Almer JD, Mummery PM. Load transfer in bovine plexiform bone determined by synchrotron X-ray diffraction. J Mater Res 2008;23:543–50.
[27] Almer JD, Stock SR. Internal strains and stresses measured in cortical bone via high-energy X-ray diffraction. J Struct Biol 2005;152:14–27.
[28] Almer JD, Stock SR. Micromechanical response of mineral and collagen phases in bone. J Struct Biol 2007;157:365–70.
[29] Gupta HS, Seto J, Wagermaier W, Zaslansky P, Boesecke P, Fratzl P. Cooperative deformation of mineral and collagen in bone at the nanoscale. Proc Natl Acad Sci 2006;103:17741–6.
[30] Akhtar R, Daymond MR, Almer JD, Mummery PM. Elastic strains in antler trabecular bone determined by synchrotron X-ray diffraction. Acta Biomater 2008;4:1677–87.
[31] Contardo L, De Luca M, Biasotto M, Longo R, Olivo A, Pani S, et al. Evaluation of the endodontic apical seal after post insertion by synchrotron radiation microtomography. Nucl Instrum Methods Phys Res Sect A 2005;548:253–6.
[32] De Santis R, Mollica F, Prisco D, Rengo S, Ambrosio L, Nicolais L. A 3D analysis of mechanically stressed dentin–adhesive–composite interfaces using X-ray microCT. Biomaterials 2005;26:257–70.
[33] Dowker S, Elliott J, Davis G, Wilson R, Cloetens P. Synchrotron X-ray microtomographic investigation of mineral concentrations at micrometer scale in sound and carious enamel. Caries Res 2004;37:514–22.
[34] Dowker S, Elliott J, Davis G, Wilson R, Cloetens P. Three-dimensional study of human fissure enamel by synchrotron X-ray microtomography. Eur J Oral Sci 2006;114:353–9.
[35] Stock SR, Vieira AEM, Delbem ACB, Cannon ML, Xiao X, De Carlo F. Synchrotron microcomputed tomography of the mature bovine dentinoenamel junction. J Struct Biol 2008;161:162–71.
[36] Huang TTY, Jones AS, He LH, Darendeliler MA, Swain MV. Characterization of enamel white spot lesions using X-ray micro-tomography. J Dent 2007;35:737–43.
[37] Tafforeau P, Bentaleb I, Jauger JJ, Martin C. Nature of laminations and mineralization in rhinoceros enamel using histology and X-ray synchrotron microtomography: potential implications for palaeoenvironmental isotopic studies. Palaeogeogr Palaeoclimateol Palaeoecol 2007;246:206–27.
[38] Grigoratos D, Knowles J, Ng YL, Gulabivala K. Effect of exposing dentine to sodium hypochlorite and calcium hydroxide on its flexural strength and elastic modulus. Int Endod J 2001;34:113–9.
[39] Marshall GW, Yücel N, Balooch M, Kinney JH, Habelitz S, Marshall SJ. Sodium hypochlorite alterations of dentin and dentin collagen. Surf Sci 2001;491:444–55.
[40] Sim TPC, Knowles JC, Ng YL, Shelton J, Gulabivala K. Effect of sodium hypochlorite on mechanical properties of dentine and tooth surface strain. Int Endod J 2001;34:120–32.
[41] Na GC. Interaction of calf skin collagen with glycerol-linked function-analysis. Biochemistry 1986;25:967–73.
[42] Na GC, Butz LJ, Bailey DG, Carroll RJ. In vitro collagen fibril assembly in glycerol solution – evidence for a helical cooperative mechanism involving microfibrils. Biochemistry 1986;25:958–66.
[43] Kuznetsova N, Chi SL, Leikin S. Sugars and polyols inhibit fibrillogenesis of type I collagen by disrupting hydrogen-bonded water bridges between the helices. Biochemistry 1998;37:11888–95.
[44] Wells PB, Yeh AT, Humphrey JD. Influence of glycerol on the mechanical reversibility and thermal damage susceptibility of collagenous tissues. IEEE Trans Biomed Eng 2006;53:747–53.
[45] Moscovich H, Creugers NHJ, Jansen JA, Wolke JGC. In vitro dentine hardness following gamma-irradiation and freezing. J Dent 1999;27:503–7.
[46] Sedlin ED. A rheological model for cortical bone: a study of the physical properties of human femoral samples. Acta Orthop Scand 1965;83(Suppl.):20–1.
[47] Tonami K-I, Takahashi H, Nishimura F. Effect of frozen storage and boiling on tensile strength of bovine dentin. Dent Mater J 1996;15:205–11.
[48] De Carlo F, Xiao X, Tieman B. X-ray tomography system, automation and remote access at beamline 2-BM of the Advanced Photon Source. In: Bonse U, editor. Developments in X-ray tomography V, vol. 6318. Bellingham (WA): SPIE; 2006. p. K3180.
[49] Wang Y, De Carlo F, Mancini D, McNulty I, Tieman B, Bresnahan J, et al. High-throughput X-ray microtomography system at the Advanced Photon Source. Rev Sci Instrum 2001;72:2062–8.
[50] Rasband W. ImageJ. Bethesda (MD): US National Institutes of Health; 1997–2008. Available from: http://rsb.info.nih.gov/ij/.
[51] Daymond MR, Young ML, Almer JD, Dunand DC. Strain and texture evolution during mechanical loading of a crack tip in martensitic shape-memory NiTi. Acta Mater 2007;55:3929–42.
[52] Wanner A, Dunand DC. Synchrotron X-ray study of bulk lattice strains in externally loaded Cu–Mo composites. Metall Mater Trans A – Phys Metall Mater Sci 2000;31:2949–62.
[53] Young ML, Almer JD, Lienert U, Haeffner DR, Rao R, Lewis JA, et al. Diffraction measurements of load transfer in interpenetrating-phase Al_2O_3/Al composites. In: Panday AB, Kendig KL, Lewandowski JJ, Shah SS, editors. Affordable metal matrix composites for high-performance applications, vol. II; 2003. p. 225–33.
[54] Hammersley AP. FIT2D: an introduction and overview. ESRF internal report 97HA02T. ESRF; 1997.
[55] Hammersley AP. FIT2D V9.129 reference manual V3.1. ESRF internal report 98HA01T. ESRF; 1998.
[56] He BB, Smith KL. In: SEM spring conference on experimental and applied mechanics and experimental/numerical mechanics in electronic packaging III, Houston (TX); 1998.
[57] Holager J. Thermogravimetric examination of enamel and dentin. J Dent Res 1970;49:546–8.
[58] Fels IG. Hydration and density of collagen and gelatin. J Appl Polym Sci 1964;8:1813–24.
[59] Gaines RV, Skinner HCW, Foord EE, Mason B, Rosenzweig A. Dana's new mineralogy: the system of mineralogy of James Dwight Dana and Edward Salisbury Dana. 8th ed. Hoboken (NJ): John Wiley & Sons; 1997.
[60] Wegehaupt F, Gries D, Wiegand A, Attin T. Is bovine dentine an appropriate substitute for human dentine in erosion/abrasion tests? J Oral Rehabil 2008;35:390–4.
[61] Fonseca RB, Haiter-Neto F, Carlo HL, Soares CJ, Sinhoreti MAC, Puppin-Rontani RM, et al. Radiodensity and hardness of enamel and dentin of human and bovine teeth, varying bovine teeth age. Arch Oral Biol 2008;53:1023–9.
[62] Fonseca RB, Haiter-Neto F, Fernandes-Neto AJ, Barbosa GAS, Soares CJ. Radiodensity of enamel and dentin of human, bovine and swine teeth. Arch Oral Biol 2004;49:919–22.
[63] Hirayama A. Experimental analytical electron microscopic studies on the quantitative analysis of elemental concentrations in biological thin specimens and its application to dental science. Shikwa Gakuho 1990;90:1019–36.
[64] Sumikawa DA, Marshall GW, Gee L, Marshall SJ. Microstructure of primary tooth dentin. Pediatr Dent 1998;21:439–44.
[65] Hosoya Y, Marshall GW. The nano-hardness and elastic modulus of sound deciduous canine dentin and young premolar dentin – preliminary study. J Mater Sci Mater Med 2005;16:1–8.
[66] Gertenbach WD. Beef production: the basics. Pietermaritzberg, South Africa: KwaZulu-Natal Department of Agriculture; 1998.
[67] Sano H, Ciucchi B, Matthews WG, Pashley DH. Tensile properties of mineralized and demineralized human and bovine dentin. J Dent Res 1994;73:1205–11.

[68] Grenoble DE, Katz JL, Dunn KL, GIlmore RS, Murty KL. The elastic properties of hard tissues and apatites. J Biomed Mater Res 1972;6:221–33.
[69] Gilmore RS, Katz JL. Elastic properties of apatites. J Mater Sci 1982;17:1131–41.
[70] Jager I, Fratzl P. Mineralized collagen fibrils: a mechanical model with a staggered arrangement of mineral particles. Biophys J 2000;79:1737–46.
[71] Bozec L, de Groot J, Odlyha M, Nicholls B, Nesbitt S, Flanagan A, et al. Atomic force microscopy of collagen structure in bone and dentine revealed by osteoclastic resorption. Ultramicroscopy 2005;105:79–89.
[72] Timshenko SP, Goodier JN. Theory of elasticity. 3rd ed. New York: McGraw-Hill; 1987.
[73] Arias JL, Mayor MB, Pou J, Leng Y, Leon B, Perez-Amor M. Micro- and nano-testing of calcium phosphate coatings produced by pulsed laser deposition. Biomaterials 2003;24:3403–8.
[74] Zhang C, Leng Y, Chen J. Elastic and plastic behavior of plasma-sprayed hydroxyapatite coatings on Ti–6Al–4V substrate. Biomaterials 2001;22:1357–63.
[75] Bertinetti L, Tampieri A, Landi E, Ducatti C, Midgley PA, Coluccia S, et al. Surface structure, hydration, and cationic sites of nanohydroxyapatite: UHR-TEM, IR, and microgravimetric studies. J Phys Chem C 2007;111:4027–35.
[76] Rusu VM, Ng CH, Wilke M, Tiersch B, Fratzl P, Martin GP. Size-controlled hydroxyapatite nanoparticles as self-organizing organic–inorganic composite materials. Biomaterials 2005;26:5414–26.
[77] Crane NJ, Popescu V, Morris MD, Steenhuis P, Ignelzi MA. Raman spectroscopic evidence for octacalcium phosphate and other transient mineral species deposited during intramembranous mineralization. Bone 2006;39:434–42.
[78] Eanes ED, Gillesse IH, Gosner AS. Intermediate states in precipitation of hydroxyapatite. Nature 1965;208:365–7.
[79] Boskey A, Camacho NP. FT-IR imaging of native and tissue-engineered bone and cartilage. Biomaterials 2007;28:2465–78.
[80] Leventouri T, Antonakos A, Kyriacou A, Venturelli R, Liarokapis E, Perdikatsis V. Crystal structure studies of human dental apatite as a function of age, vol. 0806.1233v2. Cornell University Library; 2009.
[81] Leventouri T. Synthetic and biological hydroxyapatites: crystal structure questions. Biomaterials 2006;27:3339–42.
[82] Girault B, Vidal V, Thilly L, Renault P-O, Goudeau P, Le Bourhis E, et al. Small scale mechanical properties of polycrystalline materials: in situ diffraction studies. Int J Nanotechnol 2008;5:609–29.
[83] Cao HS, Bonnet R, Hunsinger J, Elkedim O. Determination of elastic properties of consolidated nanocrystalline alloys iron–copper by means of acoustic echography and interferometry. Scr Mater 2003;48:531–7.
[84] Huang H, Spaepen F. Tensile testing of free-standing Cu, Ag, and Al thin films and Ag/Cu multilayers. Acta Mater 2000;48:3261–9.
[85] Kalkman AJ, Verbruggen AH, Janssen GCAM. Young's modulus measurements and grain boundary sliding in freestanding thin metal films. Appl Phys Lett 2001;78:2673–5.
[86] Kobelev NP, Soifer YM, Andrievski RA, Gunther B. Microhardness and elastic properties of nanocrystalline silver. Nanostruct Mater 1993;2:537–44.
[87] Kopycinske-Muller M, Geiss RH, Muller J, Hurley DC. Elastic-property measurements on ultrathin films using atomic force acoustic microscopy. Nanotechnology 2005;16:703–9.
[88] Ruud JA, Jervis TR, Spaepen F. Nanoindentation of Ag/Ni multilayered thin films. J Appl Phys 1994;75:4969–74.
[89] Schiotz J, Di Tolla FD, Jacobsen KW. Softening of nanocrystalline metals at very small grain sizes. Nature 1998;391:561–3.
[90] Villain P, Goudeau P, Renault P-O, Badawi KF. Size effect on intragranular elastic constants in thin tungsten films. Appl Phys Lett 2002;81:4365–7.
[91] Villain P, Beauchamp P, Badawi KF, Goudeau P, Renault P-O. Atomistic calculation of size effects on elastic coefficients in nanometer-sized tungsten layers and wires. Scr Mater 2004;50:1247–51.
[92] Chudoba T, Griepentrog M, Duck A, Schneider D, Richter F. Young's modulus measurements on ultra-thin coatings. J Mater Res 2004;19:301–14.
[93] Schneider D, Witke T, Schwarz T, Schoneich B, Schultrich B. Testing ultra-thin films by laser acoustics. Surf Coat Technol 2000;126:136–41.
[94] Schneider D, Siemroth P, Schulke T, Berthold J, Schultrich B, Schneider H-H, et al. Quality control of ultra-thin and super hard coatings by laser acoustics. Surf Coat Technol 2002;153:252–60.
[95] Sun CT, Zhang H. Size-dependent elastic moduli of platelike nanomaterials. J Appl Phys 2003;93:1212–8.
[96] Chen CQ, Shi Y, Zhang YS, Zhu J, Yan YJ. Size dependence of Young's modulus in ZnO nanowires. Phys Rev Lett 2006;96:75505.
[97] Stan G, Ciobanu CV, Parthangal PM, Cook RF. Diameter-dependent radial tangential elastic moduli of ZnO nanowires. Nano Lett 2008;7:3691–7.
[98] Petersen KE, Guarnieri CR. Young's modulus measurements of thin films using micromechanics. J Appl Phys 1979;50:6761–6.
[99] Teraoka K, Maekawa K, Onuma K, Tateishi T, Tsutsumi S. Mechanical properties of hydroxyapatite and OH-carbonated hydroxyapatite single crystals. J Dent Res 1998;77:1560–8.
[100] Rey C, Combes C, Drouet C, Sfihi H, Barroug A. Physico-chemical properties of nanocrystalline apatites: implications for biominerals and biomaterials. Mater Sci Eng C 2007;27:198–205.